Effect of Scale-Aware Planetary Boundary Layer Schemes on Tropical Cyclone Intensification and Structural Changes in the Gray Zone

XIAOMIN CHEN,[a] MING XUE,[b,c] BOWEN ZHOU,[a] JUAN FANG,[a] JUN A. ZHANG,[d,e] AND FRANK D. MARKS[d]

[a] *Key Laboratory for Mesoscale Severe Weather/Ministry of Education, and School of Atmospheric Sciences, Nanjing University, Nanjing, China*
[b] *Center for Analysis and Prediction of Storms, University of Oklahoma, Norman, Oklahoma*
[c] *School of Meteorology, University of Oklahoma, Norman, Oklahoma*
[d] *NOAA/AOML/Hurricane Research Division, Miami, Florida*
[e] *Cooperative Institute for Marine and Atmospheric Studies, University of Miami, Miami, Florida*

(Manuscript received 9 September 2020, in final form 5 April 2021)

ABSTRACT: Horizontal grid spacings of numerical weather prediction models are rapidly approaching $O(1)$ km and have become comparable with the dominant length scales of flows in the boundary layer; within such "gray-zones," conventional planetary boundary layer (PBL) parameterization schemes start to violate basic design assumptions. Scale-aware PBL schemes have been developed recently to address the gray-zone issue. By performing WRF simulations of Hurricane Earl (2010) at subkilometer grid spacings, this study investigates the effect of the scale-aware Shin–Hong (SH) scheme on the tropical cyclone (TC) intensification and structural changes in comparison to the non-scale-aware YSU scheme it is built upon. Results indicate that SH tends to produce a stronger TC with a more compact inner core than YSU. At early stages, scale-aware coefficients in SH gradually decrease as the diagnosed boundary layer height exceeds the horizontal grid spacing. This scale-aware effect is most prominent for nonlocal subgrid-scale vertical turbulent fluxes, in the nonprecipitation regions radially outside of a vortex-tilt-related convective rainband, and from the early stage through the middle of the rapid intensification (RI) phase. Both the scale awareness and different parameterization of the nonlocal turbulent heat flux in SH reduce the parameterized vertical turbulent mixing, which further induces stronger radial inflows and helps retain more water vapor in the boundary layer. The resulting stronger moisture convergence and diabatic heating near the TC center account for a faster inner-core contraction before RI onset and higher intensification rates during the RI period. Potential issues of applying these two PBL schemes in TC simulations and suggestions for improvements are discussed.

KEYWORDS: Turbulence; Boundary layer; Hurricanes/typhoons; Model evaluation/performance; Numerical analysis/modeling

1. Introduction

Turbulence within the tropical cyclone (TC) boundary layer is affected by the strong winds and inertial stability (e.g., Eliassen 1971; Kepert 2001), making the TC boundary layer distinct from the traditional convective boundary layer. Growing evidences have shown that parameterized boundary layer turbulent fluxes can impact TC inflow strength and depth and further modulate TC intensity change (e.g., Braun and Tao 2000; Smith and Thomsen 2010; Gopalakrishnan et al. 2013; Zhang et al. 2015). However, accurately representing turbulent fluxes in the planetary boundary layer (PBL) schemes for TC simulations remains challenging. This is in part due to the scarcity of in situ turbulence measurements in high wind conditions, especially those over the ocean, and to the fact that the existing PBL schemes are generally tuned based on observations or large-eddy simulations of convective boundary layers over land.

The issue is further complicated with the increase in computing power, which enables horizontal grid spacings (Δ) of global and regional numerical models at ~1 km or smaller (e.g., Nolan et al. 2009; Miyamoto et al. 2013; Shin and Dudhia 2016; Biswas et al. 2020). Such grid spacings are comparable to the boundary layer height (z_i) of TCs (Zhang et al. 2011b), and belongs to the "terra incognita" (Wyngaard 2004), also well known as the model gray zone (Arakawa et al. 2011). While boundary layer turbulence is completely parameterized in coarse-resolution simulations ($\Delta \gg z_i$), it becomes partially resolved by model grid points at gray-zone resolutions. Therefore, neither the traditional PBL schemes nor large-eddy simulations with subgrid-scale (SGS) turbulence closure is appropriate to represent the boundary layer turbulence in the gray zone. The direct use of traditional PBL schemes in the gray zone can result in overestimated turbulent mixing. Many ensuing unrealistic features have been reported in previous studies of the convective boundary layer, including weakened resolved motions (Honnert et al. 2011; Ching et al. 2014) and broken or thinner convective rolls (LeMone et al. 2010; Shin and Hong 2015).

To alleviate the gray-zone issue, several scale-aware PBL schemes have been developed in recent years in the

Chen's current affiliation: NOAA/AOML/Hurricane Research Division, Miami, Florida.

Corresponding author: Dr. Xiaomin Chen, xiaomin.chen@noaa.gov

Publisher's Note: This article was revised on 9 June 2021 to correct a mistake in the list of author affiliations.

DOI: 10.1175/MWR-D-20-0297.1

context of the convective boundary layer (Boutle et al. 2014; Shin and Hong 2015; Ito et al. 2015). The core essence of the scale awareness in these PBL schemes is to apply a predefined empirical partition function of the dimensionless grid spacing Δ/z_i to down-weight PBL-scheme-parameterized turbulent fluxes in the gray zone. Although these empirical functions generally lack a solid theoretical basis (Zhou et al. 2017), they have been shown to have the desired effects on the convective boundary layer. However, to the best knowledge of the authors, evaluation of the performance of such scale-aware PBL schemes in TC simulations is not found in formal literature.

This study is motivated to investigate the effect of the scale-aware PBL scheme on TC intensification and structural changes within a set of WRF simulations of Hurricane Earl (2010) at subkilometer horizontal grid spacings. The subkilometer grid spacing is selected because observational analysis of in situ dropsondes indicates that the TC boundary layer height in terms of the mixed-layer depth[1] is generally less than 1 km (Zhang et al. 2011b). Two PBL schemes are selected in this study, namely, the YSU (Hong et al. 2006) and Shin–Hong (below abbreviated as SH; Shin and Hong 2015) schemes. YSU is one of the most popular PBL schemes used for TC simulations (Kepert 2012), and SH adopts similar parameterization of turbulent fluxes as YSU but with the inclusion of scale awareness. The performance of these two PBL schemes in the gray zone has been evaluated in both the dry and moist convective boundary layers (Xu et al. 2018; Choi and Han 2020) but not for the TC boundary layer. In the TC boundary layer, the adjustment of vertical mixing in the scale-aware PBL schemes may exert an impact on the extent of gradient-wind imbalance as well as vertical profiles of thermodynamic variables in the inflow layer, which may further affect the TC structure and intensity. Given this, the specific scientific questions to be addressed in this study include the following: (i) What is the effect of the scale-aware SH scheme on the structural and intensity changes of TCs at gray-zone resolutions? (ii) When and where does the scale awareness play an important role? (iii) What is the physical mechanism responsible for the differences in the structural and intensity changes?

The remainder of the paper is organized as follows. Section 2 provides an overview of the YSU and SH schemes. The data, experiment design, and model setup are described in section 3. A brief overview of the life cycle of Hurricane Earl is presented in section 4. Section 5 analyzes the effect of the scale-aware SH scheme on the TC structural and intensity changes. The related physical mechanisms and additional suggestions to the improvement of PBL schemes for TC simulations are discussed in section 6. Concluding remarks are presented in section 7.

2. A brief comparison between the YSU and SH PBL schemes

YSU is a first-order, *K*-profile parameterization (KPP)-type PBL scheme that does not involve any prognostic equations for turbulence quantities. The subgrid-scale vertical turbulent fluxes below the diagnosed boundary layer height ($z \le z_i$) are parameterized as follows (Hong et al. 2006):

$$\overline{w'C'} = -K_c\left(\frac{\partial C}{\partial z} - \gamma_c\right) + \overline{(w'C')}_h\left(\frac{z}{z_i}\right)^3, \tag{1}$$

where C is one of the prognostic variables, including meridional and zonal winds, potential temperature, moisture, and different species of hydrometers. The term K_c is the vertical eddy diffusivity, γ_c is a correction to the local gradient, and $K_c\gamma_c$ denotes countergradient fluxes. The last term on the rhs of Eq. (1) is the entrainment flux and $\overline{w'C'}_h$ is the flux at the inversion layer. The vertical viscosity for momentum (i.e., K_m) is parameterized to fit a cubic profile from the surface layer to z_i:

$$K_m = kw_s z\left(1 - \frac{z}{z_i}\right)^2, \tag{2}$$

where k is the von Kármán constant (0.4) and w_s is the mixing-layer velocity scale. The eddy diffusivity for temperature and moisture K_t is related to K_m through Prandtl number Pr, as $K_h = K_m/\mathrm{Pr}$.

The scale awareness of the SH scheme (Shin and Hong 2015) is achieved by multiplying a function of dimensionless grid spacing ($\Delta_* = \Delta/z_i$) to the local ($\overline{w'C'}^L$) and nonlocal ($\overline{w'C'}^{\mathrm{NL}}$) turbulent fluxes, respectively. The superscripts L and NL denote local and nonlocal turbulent fluxes, respectively. The total subgrid-scale turbulent fluxes are calculated as

$$\overline{w'C'} = \overline{w'C'}^L P_L + \overline{w'C'}^{\mathrm{NL}} P_{\mathrm{NL}}, \tag{3}$$

where $\overline{w'C'}^L = -K_c\partial C/\partial z$ and $\overline{w'C'}^{\mathrm{NL}} = K_c\gamma_c + \overline{(w'C')}_h(z/z_i)^3$ for momentum and scalars. The terms P_L and P_{NL} are scale-aware coefficients for local and nonlocal turbulent fluxes, respectively. One distinct difference between the two PBL schemes is that the SH scheme adopts a three-layer nonlocal vertical heat flux profile with the maximum at $0.075z_i$ (Shin and Hong 2015) while the nonlocal vertical heat flux profile in YSU takes a cubic shape with the maximum at $0.5z_i$ (Zhou et al. 2018; Hu et al. 2019). The P_{NL} and P_L approach unity at mesoscale spacings ($\Delta_* \gg 1$) and the scale-aware PBL scheme restores to the original PBL scheme. As the model grid spacing decreases to that of large-eddy simulation (LES) ($\Delta_* \ll 1$) where large turbulent eddies are well resolved, P_{NL} and P_L are gradually tapered off. Of note, P_{NL} and P_L are different for different variables. The nonlocal and local functions for potential temperature (i.e., θ) are

$$P_{\mathrm{NL}}\left(\Delta_{*\mathrm{cs}}\right) = 0.243\frac{\left(\Delta_{*\mathrm{cs}}\right)^2 + 0.936\left(\Delta_{*\mathrm{cs}}\right)^{0.875} - 1.110}{\left(\Delta_{*\mathrm{cs}}\right)^2 + 0.312\left(\Delta_{*\mathrm{cs}}\right)^{0.875} + 0.329} + 0.757, \tag{4}$$

$$P_L(\Delta_*) = 0.28\frac{(\Delta_*)^2 + 0.87(\Delta_*)^{0.5} - 0.913}{(\Delta_*)^2 + 0.153(\Delta_*)^{0.5} + 0.278} + 0.72, \tag{5}$$

where $\Delta_{*\mathrm{cs}} = \Delta_*/C_{\mathrm{cs}}$. The term C_{cs} is a stability function, whose value depends on u_*/w_* (see Fig. 1a). The terms u_* and w_* are

[1] In both YSU and SH, the boundary layer height is defined as the mixed-layer depth where positive surface heat fluxes exist.

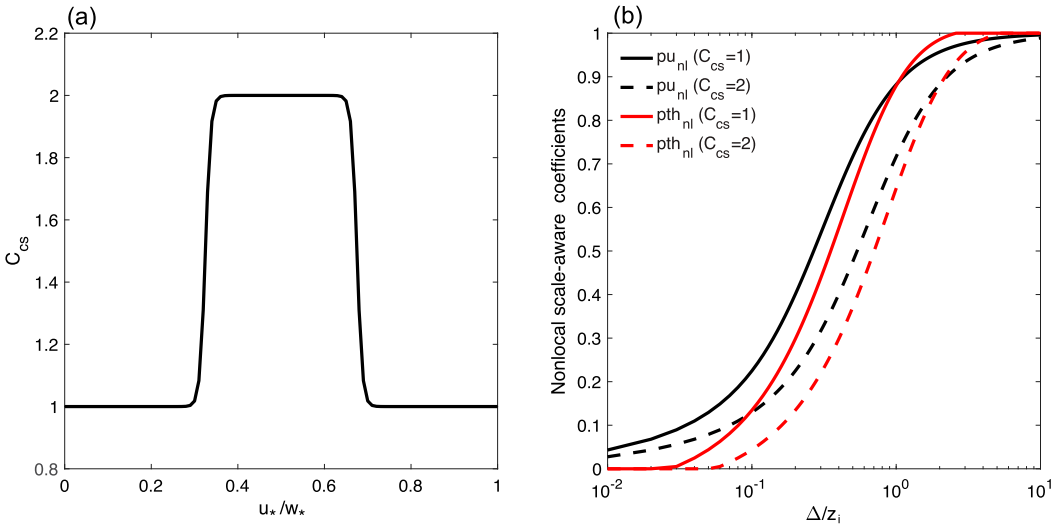

FIG. 1. (a) Stability dependency function C_{cs} in the Shin–Hong PBL scheme and (b) nonlocal scale-aware coefficient for momentum (black), and potential temperature (red) flux when $C_{cs} = 1$ (solid) or $C_{cs} = 2$ (dashed).

the surface frictional velocity and convective velocity scale, respectively. The definition of w_* is given by Hong et al. (2006) in the form of

$$w_* = \left[\frac{g}{\theta_{va}}\overline{(w'\theta'_v)}_0 h\right]^{1/3}, \tag{6}$$

where θ_{va} is the virtual potential temperature at the lowest model level and $\overline{(w'\theta'_v)}_0$ is the surface flux of virtual potential temperature. Earlier LES studies (Sykes and Henn 1989; Moeng and Sullivan 1994) have found that organized convective rolls form when $u_*/w_* \in [0.35, 0.65]$. This effect is parameterized into the scale-aware function P_{NL}, as seen from the doubled C_{cs} when $u_*/w_* \in [0.35, 0.65]$. In the gray zone, P_{NL} decreases by ~0.2 when C_{cs} increases from 1 to 2 (Fig. 1b), indicating more nonlocal turbulent fluxes being directly resolved with the existence of organized convective roll, the horizontal scale of which is 2–3z_i. The P_{NL} for momentum is slightly larger than that for θ in the gray zone.

3. Data, experiment design, and model setup

The WRF-ARW Model, version 3.8 (WRF; Skamarock and Klemp 2008) is used in this study. Two-way interactive, quadruple-nested model domains are utilized with horizontal resolutions of 12, 4, 1.33, and 0.444 km, consisting of 502 × 346, 391 × 409, 469 × 487, and 1189 × 1243 horizontal grid points, respectively (Fig. 2). The outermost domain is fixed while the inner three domains move with the model TC. All three domains contain 51 sigma levels with the top level at 50 hPa. There are 18 model levels below 850 hPa. The outer three domains run from 1800 UTC 26 August to 1800 UTC 31 August, while the innermost domain is activated 18 h later and run from 1200 UTC 27 August to 1800 UTC 31 August. The European Centre for Medium-Range Weather Forecasts interim reanalysis (ERA-Interim) data are used for the initial and lateral boundary conditions. The grid resolution of the ERA-Interim dataset is 0.702° latitude × 0.703° longitude at 37 pressure levels.

The WRF model physics configurations used are as follows: the Kain–Fritsch cumulus parameterization scheme (Kain and Fritsch 1993) in the outermost domain, the Thompson microphysics scheme (Thompson et al. 2008), the Dudhia shortwave radiation (Dudhia 1989), and the Rapid Radiative Transfer Model (RRTM) longwave radiation scheme (Mlawer et al. 1997) in all four levels of grid. The Thompson microphysics scheme is selected given recent evaluation studies using polarimetric radars indicated the Thompson scheme outperforms several other microphysics schemes by reasonably capturing raindrop size distributions and surface precipitation in TCs (e.g., Brown et al. 2016; Wu et al. 2021).

The YSU and SH PBL schemes are used in the two control simulations, named CTL-SH and CTL-YSU, respectively, and five additional sensitivity tests (see Table 1). The Revised MM5 Monin–Obukhov (below abbreviated as RMO) surface

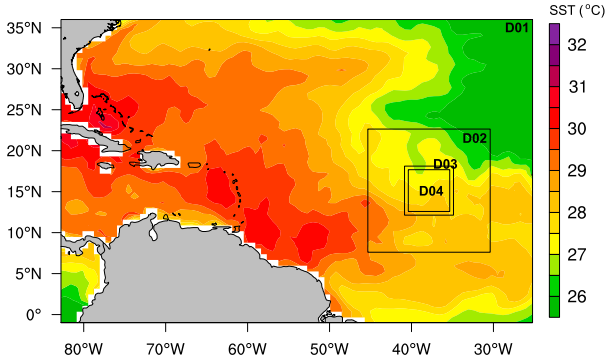

FIG. 2. Quadruple-nested model domains for the simulation of Hurricane Earl (2010). The shading denotes the sea surface temperature (°C) at 1800 UTC 26 Aug 2010.

TABLE 1. Numerical experiments design.

Expt	Description
CTL-YSU	YSU PBL scheme
CTL-SH	Shin–Hong PBL scheme
SH-NoSA	As in CTL-SH, but the scale-aware effect is turned off (i.e., $P_{NL} = P_L = 1$).
SH2YSU	As in CTL-SH, the PBL scheme is switched to YSU after 1800 UTC 29 Aug 2010.
YSU2SH	As in CTL-YSU, the PBL scheme is switched to Shin–Hong after 1800 UTC 29 Aug 2010.
lateR1-YSU	As in CTL-YSU, but the simulations start 12 h later than CTL-YSU
lateR1-SH	As in CTL-SH, but the simulations start 12 h later than CTL-SH
lateR2-YSU	As in CTL-YSU, but the simulations start 24 h later than CTL-YSU
lateR2-SH	As in CTL-SH, but the simulations start 24 h later than CTL-SH

layer scheme is adopted in both experiments. In the RMO surface layer scheme, the surface drag coefficient C_d in high winds levels off and does not continue to increase for wind speeds greater than 30 m s^{-1} (Davis et al. 2008), which is in line with the dropsonde and laboratory observations (Powell et al. 2003; Donelan et al. 2004). In all simulations, the first-order Smagorinsky closure is used for the horizontal SGS mixing, which is recommended for real-case simulations. Of note, results from one additional pair of (CTL) experiments using the WDM6 microphysics scheme (Lim and Hong 2010) are consistent with those in CTL-SH and CTL-YSU, and thus are not included in this study.

4. Overview of the evolution of Hurricane Earl (2010)

Earl (2010) originated from a tropical easterly wave that left the west coast of Africa on 23 August. With continuous convective organization in the central area of the circulation, Earl gradually intensified to a tropical depression by early 25 August and further to a tropical storm by 1200 UTC 25 August. In the next several days, it moved westward to west-northwestward under the steering flow south of the subtropical ridge. Meanwhile, it reached the hurricane intensity at 1200 UTC 29 August in an environment with warm seawater (28°–29°C, see Fig. 2) and weak-to-moderate vertical wind shear. Earl underwent a rapid intensification[2] (RI) from 0600 UTC 29 August to 1800 UTC 30 August, as it passed over the very warm seawater (~30°C). It was upgraded into a category-4 hurricane at the end of RI (Fig. 3). A concentric eyewall replacement cycle followed subsequently and the storm intensification paused. Details of the storm evolution have been reported in Cangialosi (2010) and discussed in previous literature (e.g., Montgomery et al. 2014; Rogers et al. 2015; Susca-Lopata et al. 2015; Chen and Gopalakrishnan 2015).

[2] The RI is defined as the maximum 10-m wind increasing by 15 m s^{-1} over 24 h (Kaplan and DeMaria 2003).

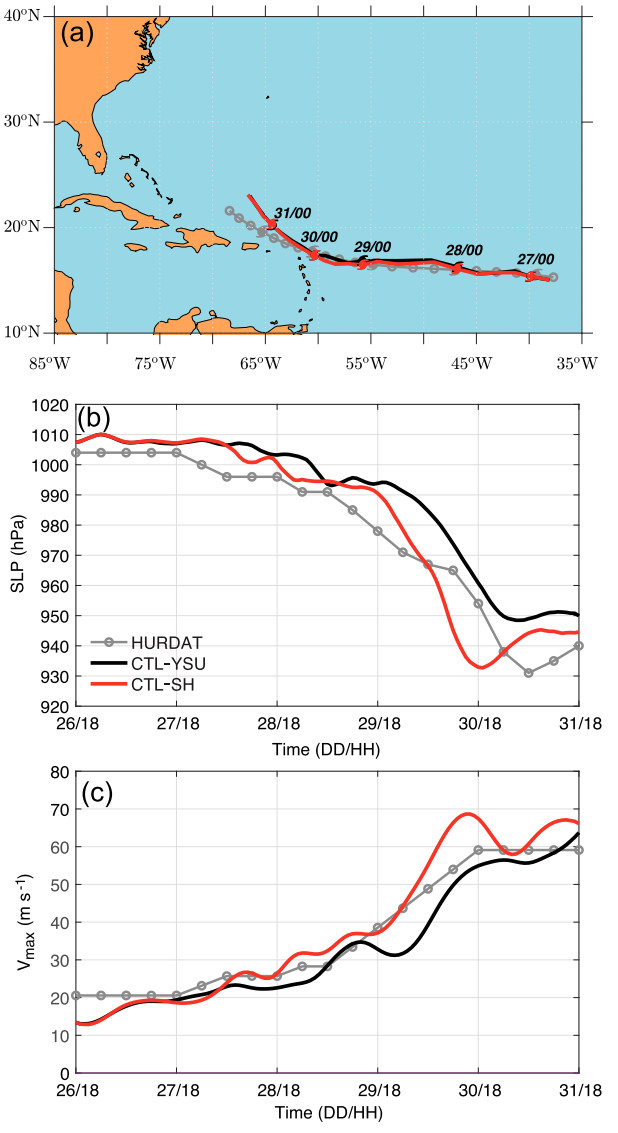

FIG. 3. Verification of the simulated (a) track, (b) minimum SLP (hPa), and (c) 10-m maximum wind speed (m s^{-1}). The gray, black, and red lines in each panel represent the best track data from the National Hurricane Center, CTL-YSU, and CTL-SH experiment, respectively.

5. Results

Figure 3 presents comparisons of track and intensity between the two control simulations (CTL-SH and CTL-YSU) and the best track from the National Hurricane Center. The RI onset in both simulations is approximately 1800 UTC 29 August, 12 h later than that in the best track data. Before RI onset, TCs in both experiments undergo several cycles of slow intensification and weakening (Fig. 3c). The weakening periods are closely related to low-level ventilation (Riemer et al. 2010), i.e., convective downdrafts bring low-θ_e air parcels from above into the boundary layer and cool the inflow layer (not shown). The low-level ventilation is unfavorable for the maintenance of convective activity within the inner-core region and TC intensification,

which has been documented in previous studies for sheared TCs (e.g., Molinari et al. 2013; Chen et al. 2019). These low-θ_e parcels are subsequently recovered by surface enthalpy fluxes and the TC intensifies again (e.g., Chen et al. 2021). The minimum sea level pressure at the peak intensity in CTL-SH is closer to the best track. During the RI period, the CTL-SH TC has a higher intensification rate than the best track while the CTL-YSU TC intensifies at a lower intensification rate. Nevertheless, both simulations generally reproduce the track, RI, and eyewall replacement cycle (not shown), and the simulation datasets provide a chance to gain insight into the effect of the scale-aware SH scheme on the TC intensity and structural changes.

a. *Impact of scale-aware SH PBL scheme on TC intensity and structural changes*

Figures 3b and 3c indicate that the intensity evolution between the two control simulations is similar until 0600 UTC 28 August. The CTL-SH TC subsequently becomes stronger than the CTL-YSU TC, and somehow the TC intensity at RI onset in the two experiments becomes comparable. Differences in the minimum sea level pressure or maximum 10-m wind speed notably increase during the RI period, i.e., from 1800 UTC 29 August to 1800 UTC 30 August. Figure 4 shows the results over the period when the innermost domain is activated. Recall that the innermost domain is activated 18 h later than the outer three domains. The evolution of the maximum 10-m axisymmetric tangential wind exhibits a similar phenomenon (Fig. 4a). The stronger CTL-SH TC after 0600 UTC 28 August is accompanied by a more rapid contraction of the radius of maximum wind (RMW) at 10-m height (Fig. 4b). The RMW of the CTL-SH TC is approximately half of the RMW of the CTL-YSU TC over the period from 0700 UTC 28 August to 0400 UTC 29 August. The increase in the TC intensity after 0600 UTC 28 August is accompanied by a steady increase in the mean boundary layer height averaged within the radius of 200 km in both experiments (Fig. 4c). Of note, the large-scale environmental vertical wind shear is very similar in CTL-YSU and CTL-SH over the simulation period (not shown) and is not responsible for driving these differences.

Figures 4a–c also show the results from the experiment SH-NoSA in which the scale-aware effect is turned off (i.e., $P_{\mathrm{NL}} = P_L = 1$). Since SH differs from YSU in both the inclusion of scale awareness and the formulation of $\overline{w'\theta'}^{\mathrm{NL}}$, this experiment is performed to separate the effects of these two different factors. Before RI onset of the CTL-SH TC, the evolution of the TC intensity and RMW at 10-m height as well as the mean boundary layer height in CTL-SH and SH-NoSA is very similar. However, the SH-NoSA TC subsequently intensifies at a much slower rate than both CTL-SH and CTL-YSU TCs. During the RI period of the CTL-SH TC, the 10-m RMW and mean boundary layer height of the SH-NoSA TC generally remain larger than those of the CTL-SH and CTL-YSU TCs. These findings suggest that during RI the higher intensification rate and smaller inner core size in CTL-SH than in CTL-YSU are mainly ascribed to the effect of scale awareness while the different parameterization of $\overline{w'\theta'}^{\mathrm{NL}}$ in SH leads to a weaker and broader TC vortex. Given $\overline{w'\theta'}^{\mathrm{NL}}$ in SH is specifically designed to work with the scale awareness at gray-zone resolutions, in the following analysis, we mainly focus on the comparison of the full scale-aware SH and the non-scale-aware YSU schemes used in CTL-SH and CTL-YSU, and discuss the effect of the scale-aware SH scheme on the TC intensity and structural change.

As the mean boundary layer height in CTL-SH becomes comparable to or larger than the horizontal grid spacing of the innermost domain (i.e., $\Delta = 444$ m), the reduction in the scale-aware coefficients becomes more notable (see discussions in section 2). Figure 4d shows the evolution of local and nonlocal scale-aware coefficients for both momentum and θ averaged within the 0–300-m layer. We select this layer to ensure that the local scale-aware coefficients are averaged within the boundary layer height. Of note, the mean boundary layer height is ~350 m prior to 0600 UTC 28 August. Figure 4d shows that the local scale-aware coefficients decrease slightly as the boundary layer height increases, while the nonlocal coefficients rapidly decrease and reach a minimum of 0.6–0.7 at nearly 1500 UTC 29 August. Given the small difference between the local and nonlocal coefficients for θ when $C_{\mathrm{cs}} = 1$ (Fig. 1b), the relatively large discrepancy between them in Fig. 4d is indicative of the modulation of the nonlocal scale-aware coefficients by the stability function ($C_{\mathrm{cs}} = 2$). This hypothesis is confirmed by Fig. 4e. The mean C_{cs} is ~1.5 before 0600 UTC 28 August and it rapidly increases toward 2.0 afterward. Consistently, the mean u_*/w_* is ~0.6 prior to 0600 UTC 28 August and subsequently decreases to ~0.45 (Fig. 4e), falling in the middle of the stability range where convective roll exists (Fig. 1a). A closer examination shows that the decrease in u_*/w_* is mainly due to the faster increase of w_* than u_* (Fig. 4f). The faster increase of w_* is traced back to 2100 UTC 27 August, which is mainly attributed to the increase of surface heat fluxes (not shown) as the near-surface winds steadily increase (Fig. 3c). The rapid growth of boundary layer height after 0600 UTC 28 August is another factor accounting for the more rapid increase of w_* [see Eq. (6)].

The nonlocal scale-aware coefficient gradually increases after 0300 UTC 30 August (i.e., in the middle of the RI period), since the mean C_{cs} steadily decreases as the mean u_*/w_* exceeds 0.65 (Fig. 4e). This is attributed to the rapid increase of the mean u_* as the storm intensifies rapidly (Fig. 4f). The above analysis demonstrates that the scale-awareness effect is most prominent through the early stage to the middle of RI, and dwindles afterward as the storm reaches major hurricane intensity.

To examine where the scale-aware effect is most significant in the TC circulation, Figs. 5a–d show the plan view of radar reflectivity and boundary layer height at 0700 UTC 28 August for the two experiments. In both experiments, a convective rainband, which is closely related to vortex tilt (not shown), is located in the front half of the storm relative to the storm motion with a left-of-motion maximum in radar reflectivity. Similar location of maximum radar reflectivity was documented in earlier observational studies for mature hurricanes (e.g., Marks 1985; Franklin et al. 1993; Reasor et al. 2000). The strongest convection is also located in the downshear-right quadrant, suggesting both the storm motion and deep-layer shear may play a role in determining the precipitation

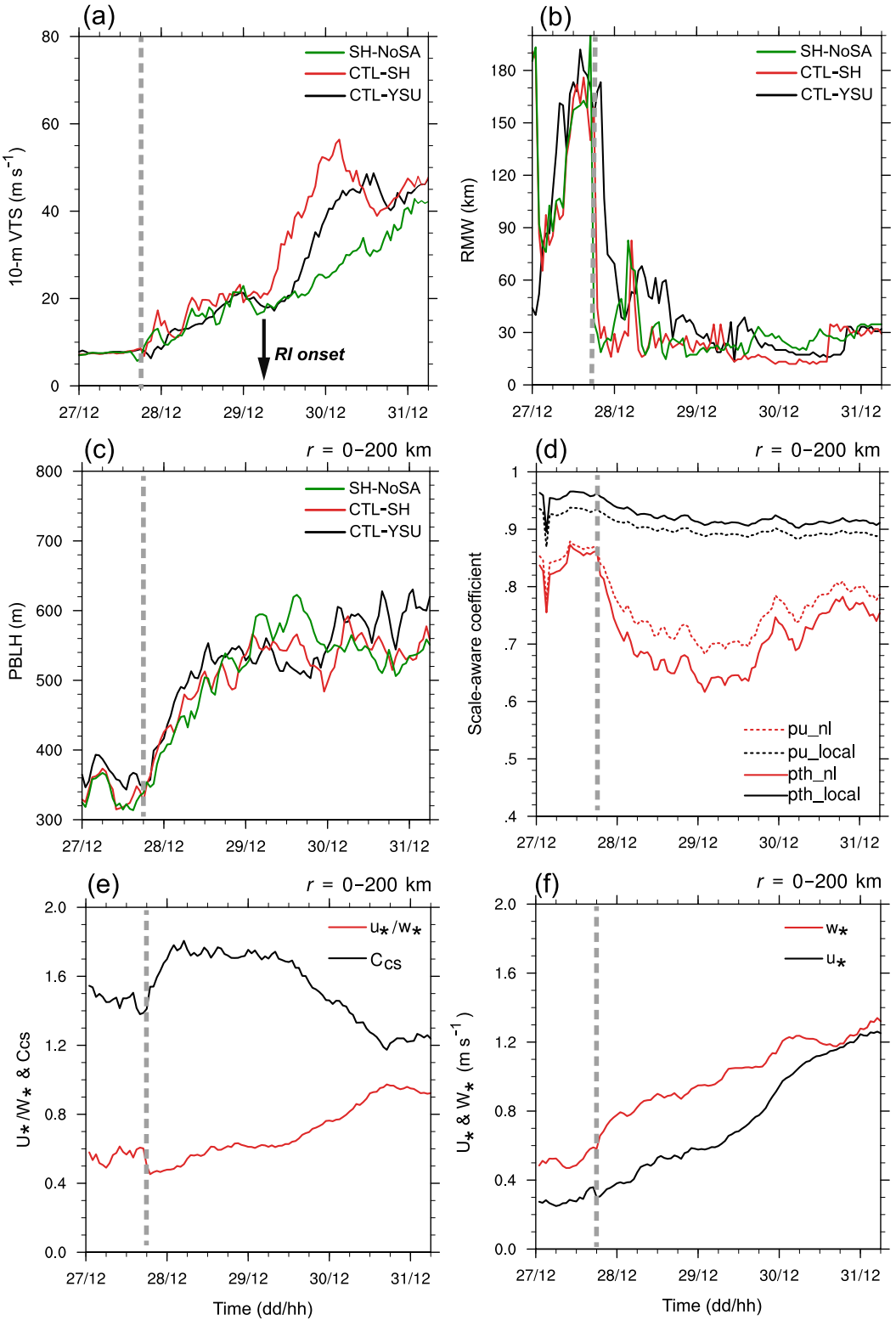

FIG. 4. Evolution of (a) maximum 10-m axisymmetric tangential wind (m s^{-1}), (b) 10-m radius of maximum wind (km), and (c) mean boundary layer height (m) in the CTL-YSU (black), CTL-SH (red), and SH-NoSA (green) experiments. Evolution of (d) mean local (black) and nonlocal (red) scale-aware coefficients for momentum (dashed) and θ (solid), (e) mean u_*/w_* (red) and C_{cs} (black), and (f) mean w_* (m s^{-1}; red) and u_* (m s^{-1}; black) in the CTL-SH experiment. The results in (c)–(f) are averaged within $r = 200$ km. The local scale-aware coefficients in (d) are averaged within the lowest 300 m. The gray dashed line in each panel denotes the time when the TC intensity of the two experiments begins to diverge. The black arrow in (a) denotes the RI onset time.

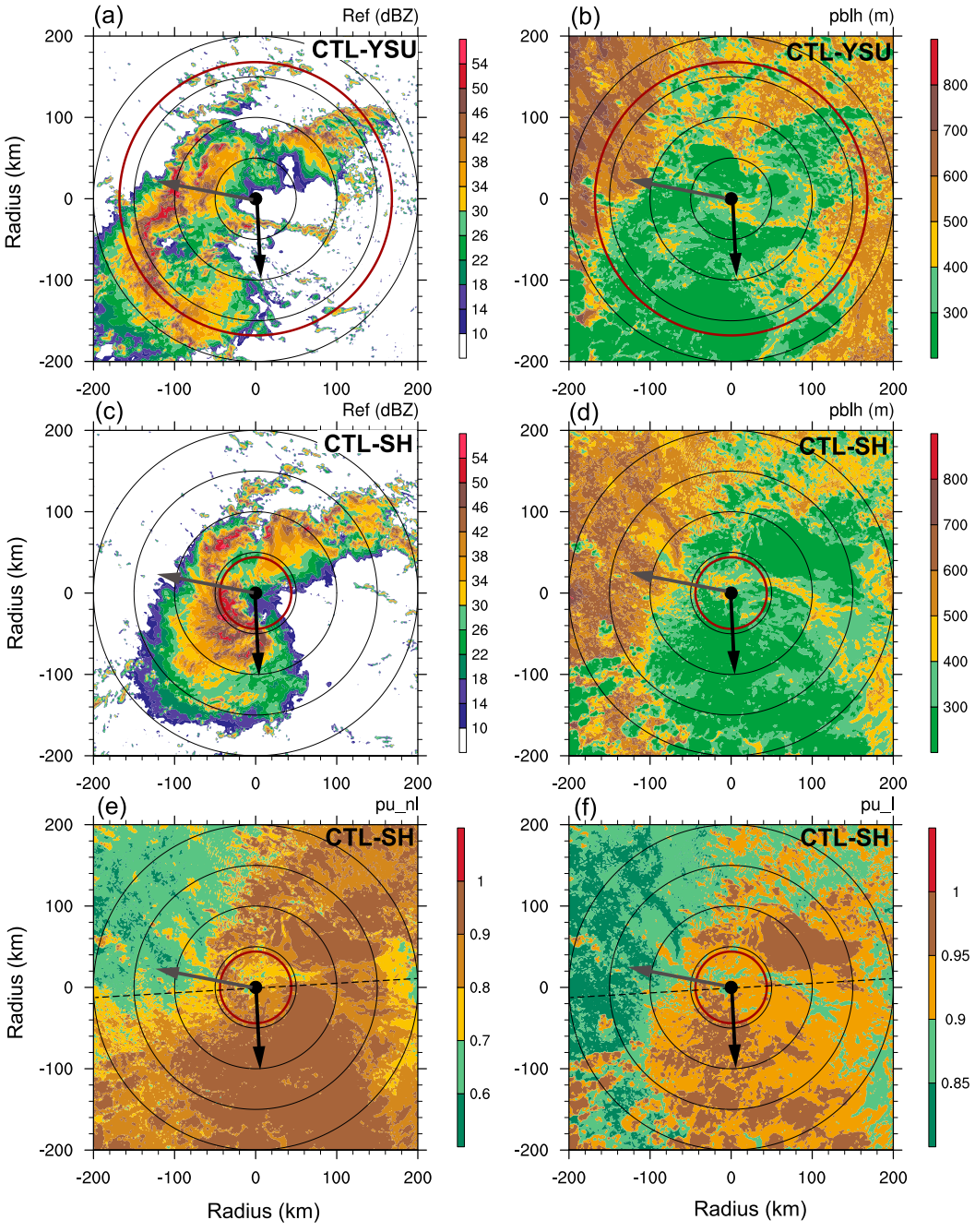

FIG. 5. Plan view of (a) radar reflectivity averaged within the lowest 500 m and (b) boundary layer height (m) at 0700 UTC 28 Aug 2010 for CTL-YSU experiment. (c),(d) As in (a) and (b), but for CTL-SH experiment. (e),(f) Plan view of nonlocal and local scale-aware coefficients for wind, respectively. The local coefficient is averaged within the lowest 300 m. Gray and black arrows denote the direction of storm motion and 200–850-hPa vertical wind shear. Dashed lines in (e) and (f) delimit the downshear and upshear semicircles. The thick red circle denotes the RMW, and the thin black circles denote the rings every 50 km.

asymmetry at the early stage. Figures 5b and 5d reveal a front-back asymmetry in the boundary layer height, which agrees with the findings of dropsonde composite analysis for hurricanes (Ren et al. 2019). The dry (i.e., nonprecipitation) region ahead of the storm and radially outward of the convective rainband has the maximum boundary layer height. Accordingly, the nonlocal and local scale-aware coefficients are smaller in the dry region, indicative of a stronger scale-aware effect.

The relationship of boundary layer height and scale-aware coefficients in the TC circulation is further examined in Fig. 6,

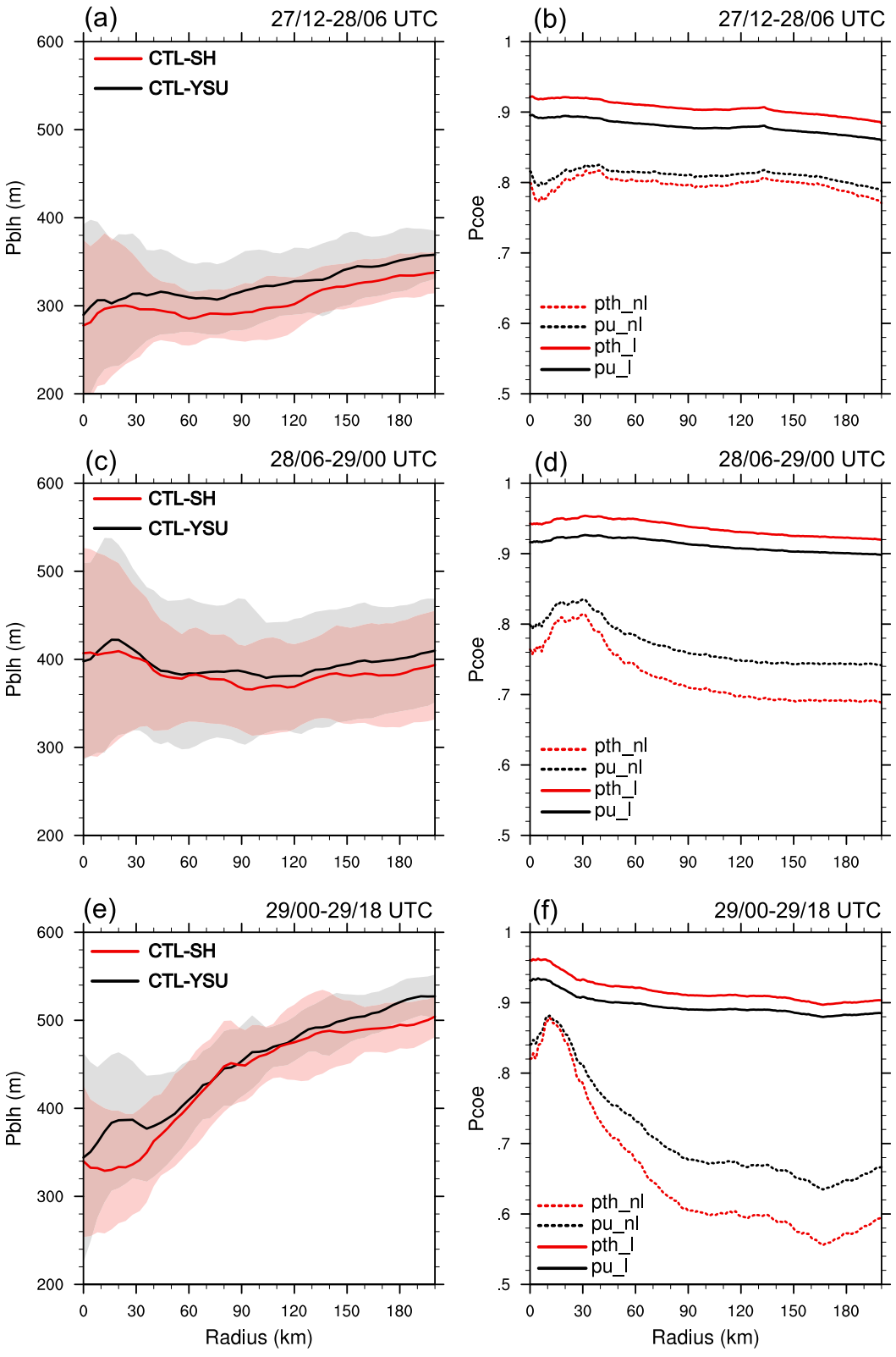

FIG. 6. The composite radial profile of (left) azimuthal-mean boundary layer height (m) and (right) scale-aware coefficients over (a),(b) 1200 UTC 27 Aug–0600 UTC 28 Aug, (c),(d) 0600 UTC 28 Aug–0000 UTC 29 Aug, and (e),(f) 0000 UTC 29 Aug–1800 UTC 29 Aug, respectively. The shading in (a), (c), and (e) represents ±1 standard deviation of the boundary layer height, and the black (red) line denotes CTL-YSU (CTL-SH). In (b), (d), and (f), P_L for momentum (black) and potential temperature (red) is averaged within the lowest 300 m. The dashed and solid lines denote P_{NL} and P_L, respectively.

which shows the composite radial profile of their azimuthal mean over three consecutive 18-h periods before RI onset and after the activation of the fourth domain. The mean boundary layer height in CTL-SH is generally shallower than that in CTL-YSU over the three periods, which is consistent with the findings in Choi and Han (2020). The boundary layer height increases with radius and correspondingly the scale-aware coefficients decrease with radius, consistent with the results shown in Fig. 5. Over periods 1 and 2 (i.e., from 1200 UTC 27 August to 0000 UTC 29 August), the radial gradient of the boundary layer height is weak within the innermost 120-km radii (Figs. 6a,c). A strong radial gradient of the boundary layer height builds up over period 3 (i.e., from 0000 UTC 29 August to 1800 UTC 29 August) immediately before RI onset, with lower values of boundary layer height at smaller radii (Fig. 6e). The sharp radial gradient of boundary layer height implies the effect of strong rotation on the mixed-layer depth or thermodynamic stability. A strong radial gradient of the scale-aware coefficients also appears over period 3 (Fig. 6f). The large discrepancy in the azimuthal-mean nonlocal and local coefficients again supports the notion that the scale-aware effect for the nonlocal fluxes is more prominent due to the modulation of the stability function C_{cs}.

Figure 7 presents the radial profiles of azimuthal-mean tangential wind, radial wind, and horizontal convergence over the same three periods. Over period 1, the profiles of tangential and radial winds in the two experiments are very similar except for the innermost 50-km radii. In CTL-SH, the tangential wind is slightly weaker and radial wind is slightly stronger within $r = 50$ km (Figs. 7a,d), and the stronger inflow corresponds to the stronger convergence therein (Fig. 7g). The stronger convergence in CTL-SH precedes stronger diabatic heating at 2-km height over period 2 (Fig. 8), indicating the role of boundary layer convergence in initiating the convection therein. The RMW of the CTL-SH TC contracts inward more rapidly and the tangential wind increases at a higher rate within $r = 50$ km (Fig. 7b) over period 2, which can be explained by a response to the stronger diabatic heating near and inside the RMW according to balanced dynamics (e.g., Shapiro and Willoughby 1982; Chen et al. 2018; Xu and Wang 2018).

The discrepancy in the magnitude of radial inflow (Fig. 7e) and convergence (Fig. 7h) between the two experiments significantly increases over period 2. The maximum convergence near the TC center in CTL-SH is nearly 2 times of that in CTL-YSU over period 2. The averaged diabatic heating near the RMW at 2-km height over period 3 (i.e., 0000 UTC 29 August–1800 UTC 29 August) is smaller than that over period 2 (Fig. 8), and the radial wind and convergence averaged in the lowest 300-m layer in CTL-SH are weaker than that over period 2 (Figs. 7f,i). Nevertheless, the CTL-SH TC still has a smaller inner core and stronger intensity than the CTL-YSU TC over period 3 (Fig. 7c).

Given that the differences in the radial inflow, horizontal convergence, and diabatic heating near the TC center between CTL-YSU and CTL-SH increase with the increasing discrepancy in vortex structure and intensity, Fig. 9 compares the vertical profiles of azimuthal-mean radial wind, specific humidity, and θ in the two experiments averaged within $r =$ 200 km over period 1, when notable differences in the vortex structure and intensity have not emerged (Figs. 4a,b and 7a,d). This comparison provides a chance to identify the impact of vertical turbulent mixing on the boundary layer structure. Figure 9a shows that the radial inflow is enhanced within z_i (≈ 350 m) (Fig. 9a), consistent with the response of the radial inflow to weaker vertical viscosity in previous studies (e.g., Gopalakrishnan et al. 2013; Zhang et al. 2015). Meanwhile, more water vapor is retained in the boundary layer of the CTL-SH TC (Fig. 9b). In CTL-SH, the stronger radial inflow carries more water vapor inward, inducing stronger horizontal convergence and diabatic heating near the TC center, as seen in Fig. 8b. Although this effect is relatively smaller over period 1, it gradually accumulates with time as the discrepancy in the vortex structure and intensity magnifies.

The stronger moisture convergence and diabatic heating at smaller radii in CTL-SH benefits a faster contraction of the low-level RMW preceding RI onset (Figs. 4b and 8). While the low-level RMW in CTL-YSU manages to contract to a similar size as that in CTL-SH at RI onset, the mean RMW of the CTL-SH TC is smaller during the RI (Fig. 4b). The faster intensification rate during the RI period in CTL-SH can be explained by the stronger boundary layer inflow and stronger diabatic heating within the more compact inner core based on an existing theory: diabatic heating at smaller radii can draw large absolute angular momentum inward to smaller radii and thereby spin up the storm circulation above the boundary layer more effectively than diabatic heating at larger radii (Smith and Montgomery 2016).

b. Sensitivity to the vortex structure at RI onset

Previous studies highlighted the importance of the inner-core structure at RI onset in the subsequent intensification (e.g., Carrasco et al. 2014; Miyamoto and Nolan 2018; Chen et al. 2018, 2019). At RI onset (i.e., 1800 UTC 29 August), the RMW in CTL-SH and CTL-YSU is very similar (Fig. 10c), while the CTL-SH TC has a much larger (~40 km) radius of gale-force winds (R17) (Fig. 10d). The different R17 may also exert an additional impact on the subsequent intensification rate and vortex structure evolution (e.g., Xu and Wang 2018). To exclude the effect of the vortex structure and clearly identify the effect of the scale-aware SH scheme in the intensity and structural evolution during the RI period, two sensitivity experiments, namely, the YSU2SH and SH2YSU (see Table 1), are performed. In experiment YSU2SH, the YSU scheme is switched to SH scheme at RI onset, and it is vice versa in SH2YSU.

The RI period in YSU2SH extends to 0300 UTC 31 August (Fig. 10b), approximately 9 h longer than in CTL-YSU, and maximum 10-m wind is ~10 m s^{-1} stronger at the end of the RI. Compared to CTL-YSU, the RMW and R17 in YSU2SH further decrease by ~4 km and ~10 km, respectively, during the RI period (Figs. 10c,d). In parallel, the comparison between CTL-SH and SH2YSU indicates that the TC intensification rate in SH2YSU is slightly reduced (Figs. 10a,b). The RMW in SH2YSU increases by ~5 km, and the R17 in SH2YSU increases by ~10 km compared to those in CTL-SH during the RI period (Figs. 10c,d). These results and the analyses in section 5a

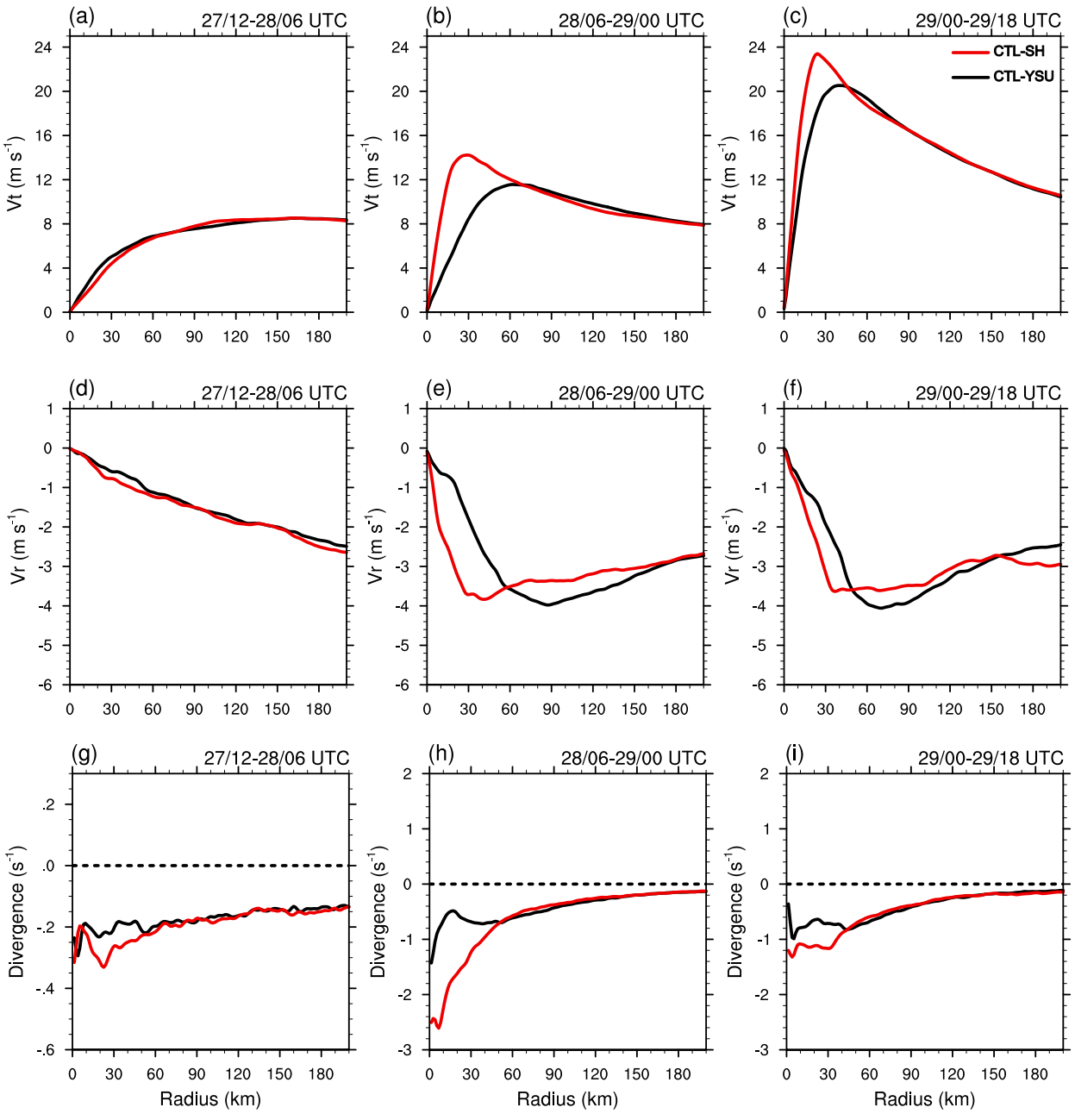

FIG. 7. Radial profile of composite (a)–(c) tangential wind, (d)–(f) radial wind ($m\,s^{-1}$), and (g)–(i) divergence ($10^{-3}\,s^{-1}$) averaged within the lowest 300 m over the same three periods as in Fig. 6. The legend for these plots is shown in (c). Note the *y* axis is different between (g) and (h)–(i).

consistently show that the SH PBL scheme tends to produce a stronger vortex with smaller inner-core size throughout the early stage to the end of RI. However, differences in the TC intensification rate by switching the PBL scheme at RI onset is much smaller than those between the two control simulations, suggesting that the vortex structure at RI onset is the main controlling factor in the rate of intensification.

Additionally, the larger radius of gale-force winds in CTL-SH than in CTL-YSU during the RI period is attributed to the differences in the vortex structure at RI onset, while the SH scheme itself tends to produce a smaller R17 if the same vortex structure as in CTL-YSU is provided at RI onset.

c. *Sensitivity to different start time*

To further test the robustness of the findings, we also run other pairs of simulations with the start time 12 h (i.e., late-R1 experiments) and 24 h (i.e., late-R2 experiments) later than the control simulations (see Table 1). The late-R1 experiments do

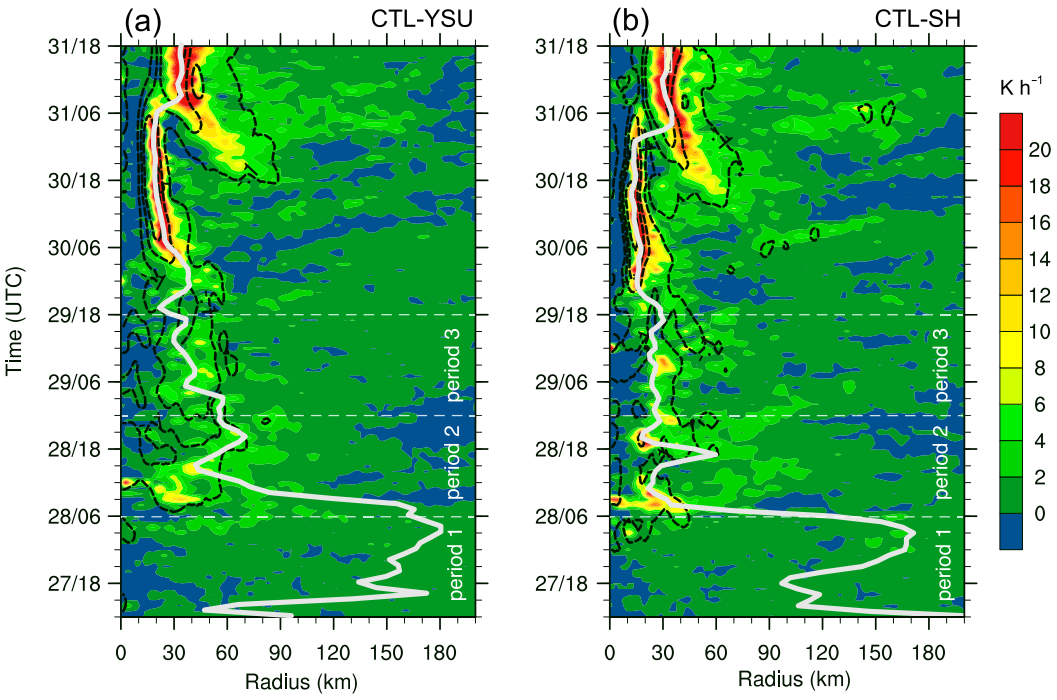

FIG. 8. Hovmöller diagram of the azimuthal-mean diabatic heating at $z = 2$ km (shading; K h^{-1}) and horizontal convergence (black contours with values of -2, -1, -0.5, -0.1×10^{-3} s^{-1}) at $z = 0.25$ km for (a) CTL-YSU and (b) CTL-SH. The thick white line in each panel denotes the RMW at $z = 0.25$ km. The white dashed lines delimit three periods before RI onset.

not show a RI until near the end of the simulations and thereby the maximum intensity of the simulated TCs is much weaker than the best track. However, at the end of the simulations, the maximum wind of the SH TC is 12 m s^{-1} larger than that of the YSU TC and the RMW of the SH TC is also smaller (not shown). The late-R2 experiments exhibit a similar RI onset timing as in CTL experiments (Fig. 11). Results consistently show that the SH TC has a smaller RMW (Fig. 11c) and exhibits higher intensification rate (Figs. 11a,b) during RI (i.e., from 0000 UTC 30 August to 0600 UTC 31 August) than the YSU TC. After 0900 UTC 31 August, the SH TC undergoes an inner-core process similar to eyewall replacement (not shown) with the RMW expanding and the intensification paused. This accounts for the fact that the SH TC is slightly weaker than the YSU TC near the end of the simulation. Nevertheless, results of the

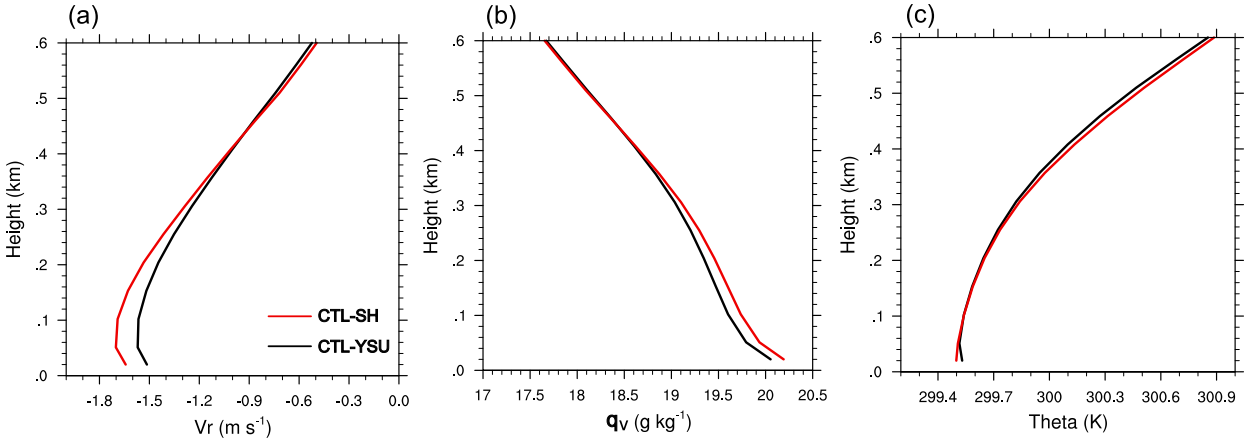

FIG. 9. Vertical profile of azimuthal-mean (a) radial wind (m s^{-1}), (b) specific humidity (g kg^{-1}), and (c) potential temperature (K) averaged within $r = 200$ km over the period from 1200 UTC 27 Aug to 0600 UTC 28 Aug 2010. The legend for these plots is shown in (a).

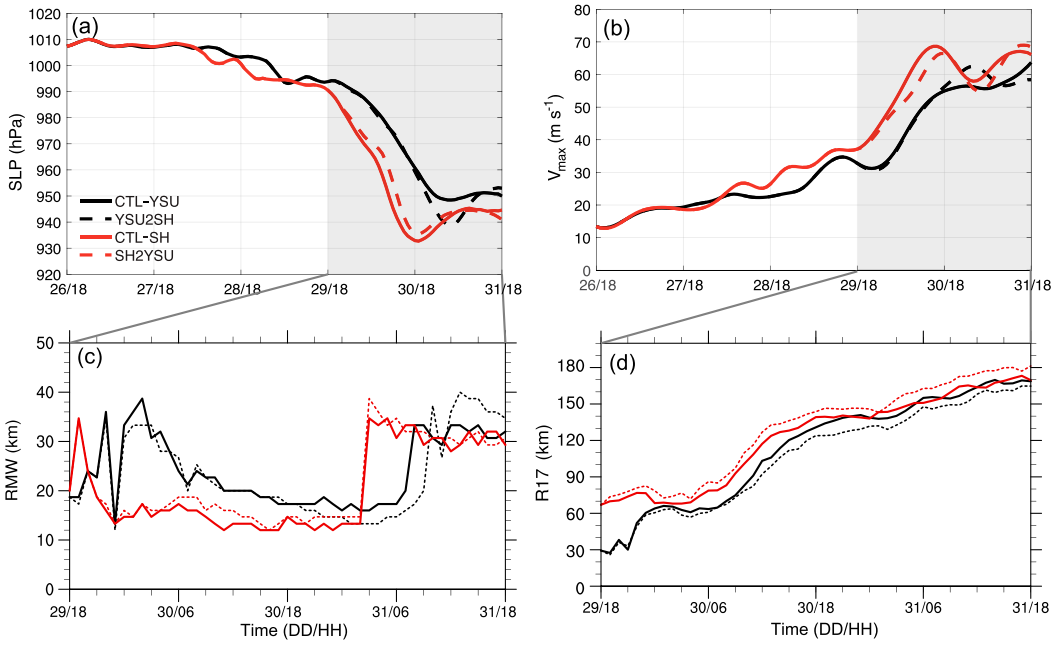

FIG. 10. Evolution of the simulated (a) minimum SLP (hPa), (b) 10-m maximum wind speed (m s^{-1}) from 1800 UTC 26 Aug to 1800 UTC 31 Aug; evolution of (c) RMW (km) and (d) radius of gale-force winds (km) from 1800 UTC 29 Aug to 1800 UTC 31 Aug. The legend for these plots is shown in (a). The gray shading in (a) and (b) denotes the analysis period in (c) and (d).

late-start simulations are generally consistent with those of the CTL simulations.

6. Discussion

a. Related mechanisms and additional discussions

The analysis in section 5 demonstrates that the scale-aware effect in SH can impact both TC intensity and structure evolutions at gray-zone resolutions. The related physical mechanism is summarized in Fig. 12. In SH, the response of the scale-aware coefficients to the changing boundary layer height leads to a dynamical adjustment of the vertical diffusivity at different stages of the TC evolution. The associated weakening in vertical turbulent mixing or increase in frictional deceleration induces stronger boundary layer inflows due to the gradient-wind imbalance in the boundary layer. The stronger radial inflows advect larger absolute angular momentum to smaller radii, which facilitates the spinup of tangential winds at smaller radii as well as a more notable RMW contraction in the TC boundary layer. Meanwhile, the weakened vertical turbulent mixing helps retain more water vapor within the boundary layer. The resulting stronger moisture convergence and diabatic heating near the TC center also help draw the large absolute angular momentum inward and spin up the TC circulation above the boundary layer more efficiently (Smith and Montgomery 2016). These physical processes account for the smaller inner core and faster intensification of the TC in CTL-SH. Of note, previous modeling studies that directly changed the vertical eddy viscosity (e.g., Gopalakrishnan et al. 2013; Zhang et al. 2015) indicated very similar physical processes.

In addition to the scale-aware effect, the weaker vertical turbulent mixing in CTL-SH is also in part attributed to the slightly lower z_i (Fig. 4c), especially before RI onset, since the maximum value of K_m is proportional to the z_i in the KPP PBL schemes (e.g., Kepert 2012). The parameterization of nonlocal vertical heat fluxes $\overline{w'\theta'}^{NL}$ in the SH scheme that has a maximum at $z = 0.075z_i$ as mentioned in section 2, while in the YSU scheme the maximum nonlocal vertical heat fluxes is maximized at $z = 0.5z_i$. Thus, in the SH scheme, the vertical turbulent mixing of θ near the surface is enhanced while the vertical turbulent mixing of θ in the mid- to upper boundary layer is weakened. The enhanced $\overline{w'\theta'}^{NL}$ near the surface accounts for the absence of the near-surface superadiabatic layer in terms of θ in CTL-SH (Fig. 9c) over period 1. The weakened vertical turbulent mixing in the mid- to upper boundary layer helps account for the slightly larger vertical gradient of θ profile in CTL-SH. Both of these two factors contribute to a lower z_i. Note that the surface heat flux in the CTL-SH and CTL-YSU experiments over period 1 (not shown) is similar and so is the θ_v excess at the lowest model level that is used to diagnose the boundary layer height [see Eq. (2) in Hong et al. 2006] in YSU and SH. As in CTL-SH, the TC in SH-NoSA also exhibits a similar lower z_i (Fig. 4c) and a similar θ profile (not shown) characterized by the absence of the near-surface superadiabatic layer and stronger vertical gradient of θ over period 1. However, the TC in SH-NoSA fails to undergo RI, which is in sharp contrast to TCs in CTL-SH and CTL-YSU,

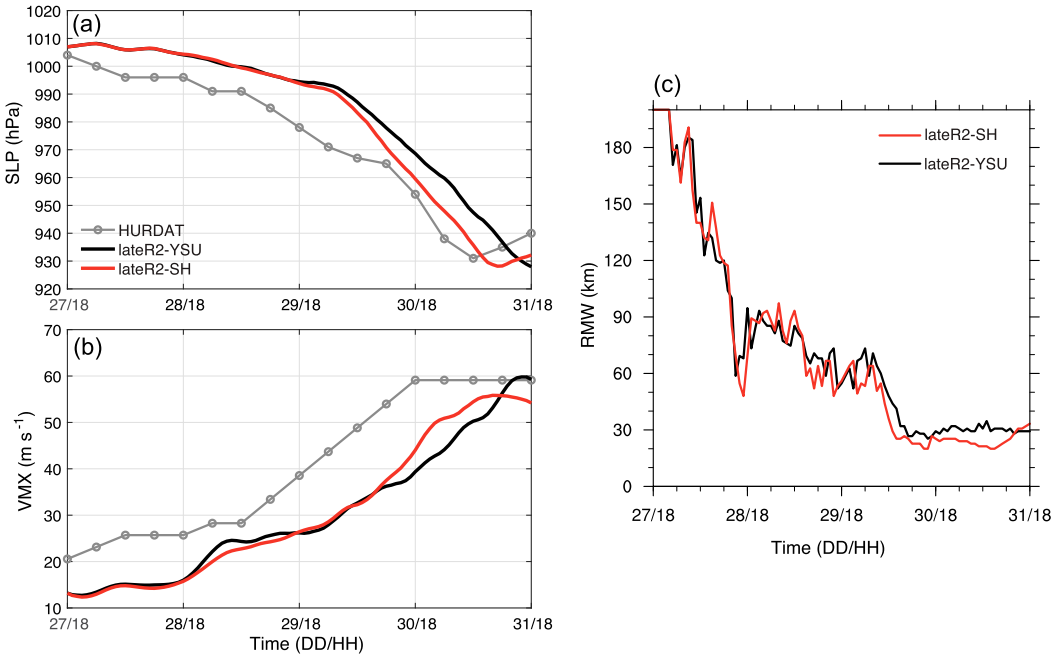

FIG. 11. Evolution of (a) minimum SLP (hPa), (b) 10-m maximum wind speed (m s^{-1}), and 10-m RMW from lateR2-YSU (black) and lateR2-SH (red) experiment. The gray line in (a) and (b) denotes the best track data from the National Hurricane Center.

indicating the dominant role of the adjustment of scale-aware coefficients in TC intensification.

b. *Suggestions for the improvement of YSU and SH schemes in TC simulations*

This study takes a preliminary step toward the understanding of scale-aware PBL parameterizations at gray-zone resolutions for TC simulations. Several potential issues of using the SH PBL schemes in the TC simulations should be noted. First, similar to YSU (Hong et al. 2006), the vertical viscosity and nonlocal turbulent fluxes in SH was formulated based on the LES of a typical convective boundary layer over land (Shin and Hong 2015), and its suitability in TC simulations is still uncertain.

Second, the enhancement of scale-aware effect within a specific range of u_*/w_* that mimics the effect of convective rolls is another potential issue. Earlier LES studies (e.g., Sykes and Henn 1989; Moeng and Sullivan 1994) that recognized the range of u_*/w_* is based on a homogeneous environmental setting, while in hurricanes the sharp radial gradient of rotational flow and the radial inflow induced by gradient-wind imbalance are indicative of a nonhomogeneous condition. One of the mechanisms responsible for the formation of roll-like structures in TC conditions is the inflection-point instability of the radial flow (e.g., Lilly 1966; Foster 2005; Morrison et al. 2005). Whether the formation of boundary layer rolls induced by the inflection-point instability is associated with the prescribed range of u_*/w_* is yet to be understood. Analytical studies indicate that the wavelength and depth of TC boundary layer roll is sensitive to the inflection-point height (Foster 2005). Further analysis into the relationship of the u_*/w_* and inflection-point height in the TC boundary layer is necessary for the improvement in the parameterization of nonlocal turbulent fluxes in SH.

Third, given that the scale-awareness parameterization in SH and the maximum vertical eddy viscosity depend crucially on the diagnosed boundary layer height (i.e., mixed-layer depth), whether the mixed-layer depth can represent the top of the boundary layer in hurricane environments is another important issue needing further investigation. In the convective boundary layer, the dominant length scale of the flow is typically assumed comparable to the boundary layer height. In this study, the mixed-layer depth in the eyewall is generally less than 800 m, while observations at the low levels of the eyewall of mature hurricanes show that the estimated horizontal length scale of the dominant turbulent eddies is mostly between 800 and 3000 m (Zhang et al. 2011a). Several earlier studies recommended using the inflow layer depth to represent the boundary layer height in hurricanes (e.g., Smith et al. 2009; Zhang et al. 2011b). This recommendation is supported by in situ momentum flux measurements (Zhang et al. 2009) in which the vertical transport of momentum flux is found to mainly occur within the inflow layer. The dropsonde composite analysis for hurricanes pointed out that the inflow layer depth is more than a factor of 2 greater than the mixed-layer depth (Zhang et al. 2011b), with a mean inflow layer depth of 1–1.5 km. The large discrepancy in the mixed-layer depth and inflow layer depth suggests choosing an appropriate TC boundary layer height in the formulations of the turbulent fluxes and scale-awareness functions is a key

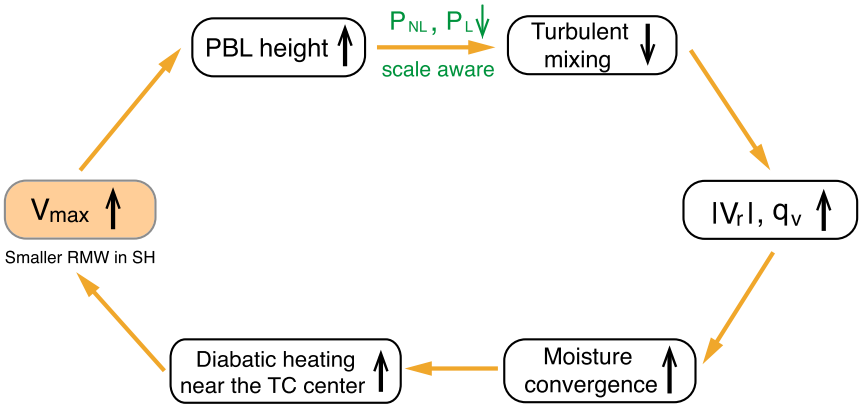

FIG. 12. Schematic of the effect of scale-awareness on TC intensification and structural changes based on the comparison of simulations with the SH and YSU PBL schemes. The V_{max} represents the maximum TC intensity, $|V_r|$ denotes the inflow strength, and q_v denotes the specific humidity.

element in the future development of KPP PBL schemes for the TC boundary layer.

7. Conclusions

This study examines the effect of a scale-aware PBL scheme on the tropical cyclone (TC) intensification and structural changes in the gray zone by performing a set of WRF-ARW simulations of Hurricane Earl (2010) at a subkilometer grid spacing (i.e., 444 m on the innermost two-way interactively nested grid). Two *K*-profile parameterization PBL schemes including nonlocal terms, i.e., the YSU and Shin–Hong (SH) schemes, are used in these simulations. SH includes the parameterization of scale dependency of the subgrid-scale (SGS) turbulence flux in the gray zone and is considered a scale-aware variation of the more traditional YSU. The essence of the scale-awareness in SH is to reduce the SGS vertical turbulence mixing in the gray zone by multiplying a function of dimensionless grid spacing (i.e., the horizontal grid spacing normalized by the boundary layer depth), since more turbulent fluxes can be explicitly resolved at finer horizontal resolutions.

Results show that the experiments using SH and YSU (i.e., CTL-SH and CTL-YSU, respectively) are capable of reproducing the rapid intensification (RI) of Earl at the gray-zone resolutions. However, the CTL-SH TC undergoes a faster intensification during the RI period and reaches a much stronger intensity after RI than the CTL-YSU TC. Additionally, the contraction of the radius of maximum wind (RMW) in CTL-SH is faster preceding RI onset, and the inner-core size remains smaller during the RI period.

Further analysis reveals that the scale-awareness starts to play a role as the diagnosed boundary layer height increases to a scale comparable with the subkilometer horizontal grid spacing. The scale-aware effect is most prominent through the early stage to the middle of RI, when nonlocal turbulent fluxes are substantially reduced due to the effect of parameterized convective rolls. In the late RI and subsequent eyewall replacement, the scale-aware effect dwindles as the nonlocal scale-aware coefficients increase. This is mainly due to the rapid increase in the surface frictional velocity during RI such that the large ratio of u_*/w_* (>0.65) becomes unfavorable for the "convective roll formation," as is parameterized in the scale-aware coefficients for nonlocal turbulent fluxes in SH. Additionally, the higher boundary layer height in the nonprecipitation region ahead of the storm and radially outward of a vortex-tilt-related convective rainband contributes to smaller scale-aware coefficients and thereby more notable reduction in the SGS turbulent fluxes.

While both the scale awareness and different parameterization of the nonlocal turbulent heat flux in SH reduce the vertical turbulent mixing, the scale awareness plays a dominant role in reducing the TC inner core size and increasing the TC intensity. The reduced vertical mixing induces stronger radial inflows and helps retain more water vapor in the lower boundary layer. The resulting stronger moisture convergence and convective diabatic heating closer to the TC center benefit faster RMW contraction before RI onset and higher intensification rates during RI. Additional sensitivity experiments that switch the PBL scheme at RI onset confirm that SH tends to produce a stronger TC with a smaller RMW during the RI period than YSU, while the vortex structure at RI onset is the controlling factor in the intensification rate during RI.

To our knowledge, this study presents a first look into the effect of a scale-aware PBL scheme on the TC intensity and structural evolution in the gray zone. As model grid spacings keep decreasing, results in this study can provide guidance for physics development of global and regional models for TC forecast purposes. Recognizing that the existing scale-aware PBL schemes are generally developed in the context of non-TC conditions, we hope this study will promote interests and attention toward the PBL scheme development for the TC boundary layer, which is quite different from the traditional continental convective boundary layer due to its predominance of shear-driven turbulence mechanisms in the lower-to-middle boundary layer (Bryan et al. 2017) as well as the effect of strong rotation on the boundary layer dynamics (Eliassen 1971;

Kepert 2001) and turbulence characteristics (Cione et al. 2020). Last, we should note that this study is based on a single case and limited model physics configurations; similar comparisons should be performed with more cases and with different model configurations to test the robustness of the results. This is a topic for future studies.

Acknowledgments. This study had been supported by the National Key R&D Program of China under Grant 2017YFC1501601 and the Natural Science Foundation of China Grant 41775056. The authors want to acknowledge Drs. Gus Alaka and Xuejin Zhang for their suggestions to improve the early version of this manuscript. The authors are also grateful for the helpful comments from two anonymous reviewers. The first author, Xiaomin Chen, is currently supported by the NRC Research Associateship Programs. Numerical simulations were performed at the High Performance Computing Center (HPCC) of Nanjing University.

REFERENCES

Arakawa, A., J. H. Jung, and C. M. Wu, 2011: Toward unification of the multiscale modeling of the atmosphere. *Atmos. Chem. Phys.*, **11**, 3731–3742, https://doi.org/10.5194/acp-11-3731-2011.

Biswas, M. K., and Coauthors, 2020: Evaluation of the Grell–Freitas convective scheme in the Hurricane Weather Research and Forecasting (HWRF) Model. *Wea. Forecasting*, **35**, 1017–1033, https://doi.org/10.1175/WAF-D-19-0124.1.

Boutle, I. A., J. E. J. Eyre, and A. P. Lock, 2014: Seamless stratocumulus simulation across the turbulent gray zone. *Mon. Wea. Rev.*, **142**, 1655–1668, https://doi.org/10.1175/MWR-D-13-00229.1.

Braun, S. A., and W.-K. Tao, 2000: Sensitivity of high-resolution simulations of Hurricane Bob (1991) to planetary boundary layer parameterizations. *Mon. Wea. Rev.*, **128**, 3941–3961, https://doi.org/10.1175/1520-0493(2000)129<3941:SOHRSO>2.0.CO;2.

Brown, B. R., M. M. Bell, and A. J. Frambach, 2016: Validation of simulated hurricane drop size distributions using polarimetric radar. *Geophys. Res. Lett.*, **43**, 910–917, https://doi.org/10.1002/2015GL067278.

Bryan, G. H., R. P. Worsnop, J. K. Lundquist, and J. A. Zhang, 2017: A simple method for simulating wind profiles in the boundary layer of tropical cyclones. *Bound.-Layer Meteor.*, **162**, 475–502, https://doi.org/10.1007/s10546-016-0207-0.

Cangialosi, J. P., 2010: Tropical cyclone report: Hurricane Earl, 25 August–4 September 2010. NOAA/NHC Tech. Rep. AL072010, 29 pp.,https://www.nhc.noaa.gov/data/tcr/AL072010_Earl.pdf.

Carrasco, C. A., C. W. Landsea, and Y.-L. Lin, 2014: The influence of tropical cyclone size on its intensification. *Wea. Forecasting*, **29**, 582–590, https://doi.org/10.1175/WAF-D-13-00092.1.

Chen, H., and S. G. Gopalakrishnan, 2015: A study on the asymmetric rapid intensification of Hurricane Earl (2010) using the HWRF system. *J. Atmos. Sci.*, **72**, 531–550, https://doi.org/10.1175/JAS-D-14-0097.1.

Chen, X., M. Xue, and J. Fang, 2018: Rapid intensification of Typhoon Mujigae (2015) under different sea surface temperatures: Structural changes leading to rapid intensification. *J. Atmos. Sci.*, **75**, 4313–4335, https://doi.org/10.1175/JAS-D-18-0017.1.

——, J. A. Zhang, and F. D. Marks, 2019: A thermodynamic pathway leading to rapid intensification of tropical cyclones in shear. *Geophys. Res. Lett.*, **46**, 9241–9251, https://doi.org/10.1029/2019GL083667.

——, J.-F. Gu, J. A. Zhang, F. D. Marks, R. F. Rogers, and J. J. Cione, 2021: Boundary layer recovery and precipitation symmetrization preceding rapid intensification of tropical cyclones under shear. *J. Atmos. Sci.*, **78**, 1523–1544, https://doi.org/10.1175/JAS-D-20-0252.1.

Ching, J., R. Rotunno, M. LeMone, A. Martilli, B. Kosovic, P. A. Jimenez, and J. Dudhia, 2014: Convectively induced secondary circulations in fine-grid mesoscale numerical weather prediction models. *Mon. Wea. Rev.*, **142**, 3284–3302, https://doi.org/10.1175/MWR-D-13-00318.1.

Choi, H.-J., and J.-Y. Han, 2020: Effect of scale-aware nonlocal planetary boundary layer scheme on lake-effect precipitation at gray-zone resolutions. *Mon. Wea. Rev.*, **148**, 2761–2776, https://doi.org/10.1175/MWR-D-19-0282.1.

Cione, J. J., and Coauthors, 2020: Eye of the storm: Observing hurricanes with a small unmanned aircraft system. *Bull. Amer. Meteor. Soc.*, **101**, E186–E205, https://doi.org/10.1175/BAMS-D-19-0169.1.

Davis, C., and Coauthors, 2008: Prediction of landfalling hurricanes with the Advanced Hurricane WRF Model. *Mon. Wea. Rev.*, **136**, 1990–2005, https://doi.org/10.1175/2007MWR2085.1.

Donelan, M. A., B. K. Haus, N. Reul, W. J. Plant, M. Stiassnie, H. C. Graber, O. B. Brown, and E. S. Saltzman, 2004: On the limiting aerodynamic roughness of the ocean in very strong winds. *Geophys. Res. Lett.*, **31**, L18306, https://doi.org/10.1029/2004GL019460.

Dudhia, J., 1989: Numerical study of convection observed during the Winter Monsoon Experiment using a mesoscale two-dimensional model. *J. Atmos. Sci.*, **46**, 3077–3107, https://doi.org/10.1175/1520-0469(1989)046<3077:NSOCOD>2.0.CO;2.

Eliassen, A., 1971: On the Ekman layer in a circular vortex. *J. Meteor. Soc. Japan*, **49A**, 784–789, https://doi.org/10.2151/jmsj1965.49A.0_784.

Foster, R. C., 2005: Why rolls are prevalent in the hurricane boundary layer. *J. Atmos. Sci.*, **62**, 2647–2661, https://doi.org/10.1175/JAS3475.1.

Franklin, J. L., S. J. Lord, S. E. Feuer, and F. D. Marks Jr., 1993: The kinematic structure of Hurricane Gloria (1985) determined from nested analyses of dropwindsonde and Doppler radar data. *Mon. Wea. Rev.*, **121**, 2433–2451, https://doi.org/10.1175/1520-0493(1993)121<2433:TKSOHG>2.0.CO;2.

Gopalakrishnan, S. G., F. Marks, J. A. Zhang, X. Zhang, J.-W. Bao, and V. Tallapragada, 2013: A study of the impacts of vertical diffusion on the structure and intensity of the tropical cyclones using the high-resolution HWRF system. *J. Atmos. Sci.*, **70**, 524–541, https://doi.org/10.1175/JAS-D-11-0340.1.

Hong, S.-Y., Y. Noh, and J. Dudhia, 2006: A new vertical diffusion package with an explicit treatment of entrainment processes. *Mon. Wea. Rev.*, **134**, 2318–2341, https://doi.org/10.1175/MWR3199.1.

Honnert, R., V. Masson, and F. Couvreux, 2011: A diagnostic for evaluating the representation of turbulence in atmospheric models at the kilometric scale. *J. Atmos. Sci.*, **68**, 3112–3131, https://doi.org/10.1175/JAS-D-11-061.1.

Hu, X.-M., M. Xue, and X. Li, 2019: The use of high-resolution sounding data to evaluate and optimize non-local PBL schemes for simulating the slightly stable upper convective boundary layer. *Mon. Wea. Rev.*, **147**, 3825–3841, https://doi.org/10.1175/MWR-D-19-0085.1.

Ito, J., H. Niino, M. Nakanishi, and C.-H. Moeng, 2015: An extension of the Mellor–Yamada model to the terra incognita zone for dry convective mixed layers in the free convection

regime. *Bound.-Layer Meteor.*, **157**, 23–43, https://doi.org/10.1007/s10546-015-0045-5.

Kain, J. S., and J. M. Fritsch, 1993: Convective parameterization for mesoscale models: The Kain–Fritsch scheme. *The Representation of Cumulus Convection in Numerical Models*, *Meteor. Monogr.*, No. 24, Amer. Meteor. Soc., 165–170.

Kaplan, J., and M. DeMaria, 2003: Large-scale characteristics of rapidly intensifying tropical cyclones in the North Atlantic basin. *Wea. Forecasting*, **18**, 1093–1108, https://doi.org/10.1175/1520-0434(2003)018<1093:LCORIT>2.0.CO;2.

Kepert, J., 2001: The dynamics of boundary layer jets within the tropical cyclone core. Part I: Linear theory. *J. Atmos. Sci.*, **58**, 2469–2484, https://doi.org/10.1175/1520-0469(2001)058<2469:TDOBLJ>2.0.CO;2.

——, 2012: Choosing a boundary layer parameterization for tropical cyclone modeling. *Mon. Wea. Rev.*, **140**, 1427–1445, https://doi.org/10.1175/MWR-D-11-00217.1.

LeMone, M. A., and Coauthors, 2010: Simulating the IHOP_2002 fair-weather CBL with the WRF-ARW–Noah modeling system. Part I: Surface fluxes and CBL structure and evolution along the eastern track. *Mon. Wea. Rev.*, **138**, 722–744, https://doi.org/10.1175/2009MWR3003.1.

Lilly, D. K., 1966: On the instability of Ekman boundary flow. *J. Atmos. Sci.*, **23**, 481–494, https://doi.org/10.1175/1520-0469(1966)023<0481:OTIOEB>2.0.CO;2.

Lim, K.-S. S., and S.-Y. Hong, 2010: Development of an effective double-moment cloud microphysics scheme with prognostic cloud condensation nuclei (CCN) for weather and climate models. *Mon. Wea. Rev.*, **138**, 1587–1612, https://doi.org/10.1175/2009MWR2968.1.

Marks, F. D., Jr., 1985: Evolution of the structure of precipitation in Hurricane Allen (1980). *Mon. Wea. Rev.*, **113**, 909–930, https://doi.org/10.1175/1520-0493(1985)113<0909:EOTSOP>2.0.CO;2.

Miyamoto, Y., and D. S. Nolan, 2018: Structural changes preceding rapid intensification in tropical cyclones as shown in a large ensemble of idealized simulations. *J. Atmos. Sci.*, **75**, 555–569, https://doi.org/10.1175/JAS-D-17-0177.1.

——, Y. Kajikawa, R. Yoshida, T. Yamaura, H. Yashiro, and H. Tomita, 2013: Deep moist atmospheric convection in a subkilometer global simulation. *Geophys. Res. Lett.*, **40**, 4922–4926, https://doi.org/10.1002/grl.50944.

Mlawer, E. J., S. J. Taubman, P. D. Brown, M. J. Iacono, and S. A. Clough, 1997: Radiative transfer for inhomogeneous atmospheres: RRTM, a validated correlated-k model for the longwave. *J. Geophys. Res.*, **102**, 16 663–16 682, https://doi.org/10.1029/97JD00237.

Moeng, C.-H., and P. P. Sullivan, 1994: A comparison of shear- and buoyancy-driven planetary boundary layer flows. *J. Atmos. Sci.*, **51**, 999–1022, https://doi.org/10.1175/1520-0469(1994)051<0999:ACOSAB>2.0.CO;2.

Molinari, J., J. Frank, and D. Vollaro, 2013: Convective bursts, downdraft cooling, and boundary layer recovery in a sheared tropical storm. *Mon. Wea. Rev.*, **141**, 1048–1060, https://doi.org/10.1175/MWR-D-12-00135.1.

Montgomery, M. T., J. A. Zhang, and R. K. Smith, 2014: An analysis of the observed low-level structure of rapidly intensifying and mature Hurricane Earl (2010). *Quart. J. Roy. Meteor. Soc.*, **140**, 2132–2146, https://doi.org/10.1002/qj.2283.

Morrison, I., S. Businger, F. Marks, P. Dodge, and J. A. Businger, 2005: An observational case for the prevalence of roll vortices in the hurricane boundary layer. *J. Atmos. Sci.*, **62**, 2662–2673, https://doi.org/10.1175/JAS3508.1.

Nolan, D. S., J. A. Zhang, and D. P. Stern, 2009: Evaluation of planetary boundary layer parameterizations in tropical cyclones by comparison of in situ observations and high-resolution simulations of Hurricane Isabel (2003). Part I: Initialization, maximum winds, and the outer-core boundary layer. *Mon. Wea. Rev.*, **137**, 3651–3674, https://doi.org/10.1175/2009MWR2785.1.

Powell, M. D., P. J. Vickery, and T. A. Reinhold, 2003: Reduced drag coefficient for high wind speeds in tropical cyclones. *Nature*, **422**, 279–283, https://doi.org/10.1038/nature01481.

Reasor, P. D., M. T. Montgomery, F. D. Marks Jr., and J. F. Gamache, 2000: Low-wavenumber structure and evolution of the hurricane inner core observed by airborne dual-Doppler radar. *Mon. Wea. Rev.*, **128**, 1653–1680, https://doi.org/10.1175/1520-0493(2000)128<1653:LWSAEO>2.0.CO;2.

Ren, Y., J. A. Zhang, S. R. Guimond, and X. Wang, 2019: Hurricane boundary layer height relative to storm motion from GPS dropsonde composites. *Atmosphere*, **10**, 339, https://doi.org/10.3390/atmos10060339.

Riemer, M., M. T. Montgomery, and M. E. Nicholls, 2010: A new paradigm for intensity modification of tropical cyclones: Thermodynamic impact of vertical wind shear on the inflow layer. *Atmos. Chem. Phys.*, **10**, 3163–3188, https://doi.org/10.5194/acp-10-3163-2010.

Rogers, R. F., P. D. Reasor, and J. A. Zhang, 2015: Multiscale structure and evolution of Hurricane Earl (2010) during rapid intensification. *Mon. Wea. Rev.*, **143**, 536–562, https://doi.org/10.1175/MWR-D-14-00175.1.

Shapiro, L. J., and H. E. Willoughby, 1982: The response of balanced hurricanes to local sources of heat and momentum. *J. Atmos. Sci.*, **39**, 378–394, https://doi.org/10.1175/1520-0469(1982)039<0378:TROBHT>2.0.CO;2.

Shin, H. H., and S.-Y. Hong, 2015: Representation of the subgrid-scale turbulent transport in convective boundary layers at gray-zone resolutions. *Mon. Wea. Rev.*, **143**, 250–271, https://doi.org/10.1175/MWR-D-14-00116.1.

——, and J. Dudhia, 2016: Evaluation of PBL parameterizations in WRF at subkilometer grid spacings: Turbulence statistics in the dry convective boundary layer. *Mon. Wea. Rev.*, **144**, 1161–1177, https://doi.org/10.1175/MWR-D-15-0208.1.

Skamarock, W. C., and J. B. Klemp, 2008: A time-split nonhydrostatic atmospheric model for weather research and forecasting applications. *J. Comput. Phys.*, **227**, 3465–3485, https://doi.org/10.1016/j.jcp.2007.01.037.

Smith, R. K., and G. L. Thomsen, 2010: Dependence of tropical-cyclone intensification on the boundary-layer representation in a numerical model. *Quart. J. Roy. Meteor. Soc.*, **136**, 1671–1685, https://doi.org/10.1002/qj.687.

——, and M. T. Montgomery, 2016: The efficiency of diabatic heating and tropical cyclone intensification. *Quart. J. Roy. Meteor. Soc.*, **142**, 2081–2086, https://doi.org/10.1002/qj.2804.

——, ——, and N. Van Sang, 2009: Tropical cyclone spin-up revisited. *Quart. J. Roy. Meteor. Soc.*, **135**, 1321–1335, https://doi.org/10.1002/qj.428.

Susca-Lopata, G., J. Zawislak, E. J. Zipser, and R. F. Rogers, 2015: The role of observed environmental conditions and precipitation evolution in the rapid intensification of Hurricane Earl (2010). *Mon. Wea. Rev.*, **143**, 2207–2223, https://doi.org/10.1175/MWR-D-14-00283.1.

Sykes, R. I., and D. S. Henn, 1989: Large-eddy simulation of turbulent sheared convection. *J. Atmos. Sci.*, **46**, 1106–1118, https://doi.org/10.1175/1520-0469(1989)046<1106:LESOTS>2.0.CO;2.

Thompson, G., P. R. Field, R. M. Rasmussen, and W. D. Hall, 2008: Explicit forecasts of winter precipitation using an improved

bulk microphysics scheme. Part II: Implementation of a new snow parameterization. *Mon. Wea. Rev.*, **136**, 5095–5115, https://doi.org/10.1175/2008MWR2387.1.

Wu, D., F. Zhang, X. Chen, A. Ryzhkov, K. Zhao, M. Kumjian, X. Chen, and P. Chan, 2021: Evaluation of microphysics schemes in tropical cyclones using polarimetric radar observations: Convective precipitation in an outer rainband. *Mon. Wea. Rev.*, **149**, 1055–1068, https://doi.org/10.1175/MWR-D-19-0378.1.

Wyngaard, J. C., 2004: Toward numerical modeling in the "terra incognita." *J. Atmos. Sci.*, **61**, 1816–1826, https://doi.org/10.1175/1520-0469(2004)061<1816:TNMITT>2.0.CO;2.

Xu, H., Y. Wang, and M. Wang, 2018: The performance of a scale-aware nonlocal PBL scheme for the subkilometer simulation of a deep CBL over the Taklimakan Desert. *Adv. Meteor.*, **2018**, 8759594, https://doi.org/10.1155/2018/8759594.

Xu, J., and Y. Wang, 2018: Effect of the initial vortex structure on intensification of a numerically simulated tropical cyclone. *J. Meteor. Soc. Japan*, **96**, 111–126, https://doi.org/10.2151/jmsj.2018-014.

Zhang, J. A., W. M. Drennan, P. G. Black, and J. R. French, 2009: Turbulence structure of the hurricane boundary layer between the outer rainbands. *J. Atmos. Sci.*, **66**, 2455–2467, https://doi.org/10.1175/2009JAS2954.1.

——, F. D. Marks, M. T. Montgomery, and S. Lorsolo, 2011a: An estimation of turbulent characteristics in the low-level region of intense Hurricanes Allen (1980) and Hugo (1989). *Mon. Wea. Rev.*, **139**, 1447–1462, https://doi.org/10.1175/2010MWR3435.1.

——, R. F. Rogers, D. S. Nolan, and F. D. Marks, 2011b: On the characteristic height scales of the hurricane boundary layer. *Mon. Wea. Rev.*, **139**, 2523–2535, https://doi.org/10.1175/MWR-D-10-05017.1.

——, D. S. Nolan, R. F. Rogers, and V. Tallapragada, 2015: Evaluating the impact of improvements in the boundary layer parameterization on hurricane intensity and structure forecasts in HWRF. *Mon. Wea. Rev.*, **143**, 3136–3155, https://doi.org/10.1175/MWR-D-14-00339.1.

Zhou, B., M. Xue, and K. Zhu, 2017: A grid-refinement-based approach for modeling the convective boundary layer in the gray zone: A pilot study. *J. Atmos. Sci.*, **74**, 3497–3513, https://doi.org/10.1175/JAS-D-16-0376.1.

——, S. Sun, K. Yao, and K. Zhu, 2018: Reexamining the gradient and countergradient representation of the local and nonlocal heat fluxes in the convective boundary layer. *J. Atmos. Sci.*, **75**, 2317–2336, https://doi.org/10.1175/JAS-D-17-0198.1.